Journal of Materials Chemistry C



COMMUNICATION

View Article Online
View Journal



Cite this: DOI: 10.1039/c9tc06145b

Received 9th November 2019, Accepted 20th December 2019

DOI: 10.1039/c9tc06145b

rsc.li/materials-c

Sc₃N@C₈₀ and La@C₈₂ doped graphene for a new class of optoelectronic devices†

High-performance hybrid graphene photodetectors were prepared with endohedral fullerenes deposited on graphene using electrophoretic methods for the first time. Endohedral Sc₃N@C₈₀, which acts as an electron acceptor, was used and the ensuing electronic and optoelectronic properties were measured. Another endohedral fullerene, La@C82, was also adsorbed on graphene, which acts as an electron donor. Upon optical illumination, for the Sc₃N@C₈₀−graphene hybrid, the photoinduced free holes are injected into graphene, increasing the hole carrier concentration in graphene, while the photoexcited electrons remain in Sc₃N@C₈₀; this leads to a high photoresponsivity \mathscr{R} of $\sim 10^9$ A W⁻¹, detectivity D of $\sim 10^{15}$ Jones, and external quantum efficiency EQE $\sim 10^9\,\%$ for the Sc₃N@C₈₀-graphene hybrid. This \mathscr{R} is ~ 10 times higher compared to other reports of quantum dot-graphene and few layer MoS2-graphene heterostructures. Similarly, for the La@C₈₂-graphene hybrid, $\mathcal{R} \sim 10^8 \text{ A W}^{-1}$, $D \sim 10^{14}$ Jones, and EQE $\sim 10^6$ % were achieved, with electrons being injected into graphene. The exceptional performance gains achieved with both types of hybrid structures confirms the potential of endohedrals to dope graphene for high performance optoelectronic devices using a facile and scalable fabrication process.

1. Introduction

Graphene, with its excellent electronic and optoelectronic properties, is a material of immense technological importance. ^{1–3}

In particular, its extremely high carrier mobility of $\sim 200\,000$ cm² V⁻¹ s⁻¹ and potential for ballistic transport⁴ provide opportunities for high-speed field-effect transistors (FETs),⁵ compared with silicon-based FETs.⁶ For its use in light detection, Sun et al.4 demonstrated the first ultrafast graphene photodetector in 2010 with extremely high operational bandwidth that resulted from its outstanding electronic properties and gapless nature. However, the responsivity \mathcal{R} of pristine graphene photodetectors is limited to $\sim 10^{-3} \text{ A W}^{-1}$ due to its poor light absorption cross-section in active regions, short photon-generated carrier lifetimes which range in the tens of picoseconds, and the absence of a gain mechanism.⁷ To overcome these challenges and enhance optical absorption, integrating semiconducting light absorbers with graphene is a viable approach for realizing high-performance graphenebased photodetectors, in which the fast exciton recombination is also minimized. Although the improvement in \mathcal{R} is substantial, the performance is still not sufficient for light detection at low-intensity illumination (in the pW range), but Roy et al.8 reported a MoS₂-graphene hybrid photodetector which yielded $\mathcal{R} \sim 10^8 \text{A W}^{-1}$ at low-intensities, down to the pW regime. After this, reports were published in rapid succession on highly sensitive photodetectors or photo-memory devices produced by hybridizing two-dimensional (2D) materials.9

For nanocarbon-based hybrids, photodetection using combinations of fullerenes (C_{60})–graphene, $^{10-17}$ C_{60} –nanoribbons, 13 transition-metal dichalcogenides (TMDC)–graphene, $^{18-20}$ TMDC– C_{60} , 14 C_{60} –hexagonal boron nitride, 11,21,22 superatomic crystals (C_{60} and metal chalcogenides crystals), 23 fluorographene, 24 iron chloride (FeCl₃)–graphene 25 have been reported. C_{60} and its derivatives, *e.g.*, [6,6]-phenyl- C_{61} -butyric acid methyl ester (PC₆₁BM) have long been employed in solar cells because of their excellent electron-accepting abilities. 26 Endohedral fullerenes can be divided into two main groups. The first include compounds that contain atoms of non-metals or simple molecules (*e.g.*, nitrogen, phosphorus, helium, xenon, *etc.*). The second group includes endohedral fullerenes which encapsulate metal ions or metal-containing clusters. 27,28 The discovery of

^a Department of Materials Science and Engineering, PACCAR Technology Institute, University of North Texas, Denton, TX 76203, USA. E-mail: anupama.kaul@unt.edu

b Department of Metallurgical, Materials and Biomedical Engineering, University of Texas at El Paso, El Paso, TX 79968, USA

^c Department of Electrical Engineering, University of Texas at El Paso, El Paso, TX 79968. USA

^d Department of Chemistry, University of Texas at El Paso, El Paso, TX 79968, USA. E-mail: echegoyen@utep.edu

^e Department of Electrical Engineering, University of North Texas, Denton, TX 76203. USA

 $[\]dagger$ Electronic supplementary information (ESI) available. See DOI: 10.1039/c9tc06145b

[‡] These authors contributed equally to the work.

endohedral cluster fullerenes in 1999 signalled a significant turning point in fullerene research, favoured by the high synthetic yields achieved and the interest in their fundamental chemical and electronic properties.²⁷

For exploring the interactions with graphene, we selected a cluster endohedral fullerene, Sc₃N@C₈₀, denoted as END₁ here, and monometallic endohedral fullerene, La@C82, denoted as END₂ here, based on their electron-accepting and electrondonating abilities, respectively.²⁸ The END₁ is very stable under ambient conditions and can be produced in high yields.²⁹⁻³¹ Similar to C₆₀, END₁ has also been used as an electron-acceptor in organic photovoltaic (OPV) cells to enhance power conversion efficiencies. 32-34 Recently, Xu et al. 35 reported the first successful and facile preparation of micron-sized hexagonal single crystalline END1 rods using the liquid-liquid interfacial precipitation (LLIP) method for photo-electrochemical applications, which clearly demonstrates its efficient charge carrier transport properties and confirms its potential for photoelectric conversion.

The END₂ in this work is also produced by the carbon arc method but the yield is far lower.³⁶ END₂ features a large anionic π surface and an open-shell structure. Importantly, in comparison to the C₆₀ absorption spectrum with peaks between the $\sim 400-700$ nm range³⁷ and the END₁ absorption spectrum between ~ 450 –680 nm, 38 the broad absorption of END₂ from ~600-1100 nm clearly highlights its enhanced optical absorption well into the infra-red regime.39 While bonding and dynamics of metal atoms inside the endohedral cages have been examined in the past, END₂ has received comparatively little attention owing largely to its lower production yields. 40,41

Despite the potential advantage of endohedrals in OPV, their integration in graphene-based devices remains essentially unexplored. Herein, for the first time, we report the combination of zero-dimensional (0D) END₁ and END₂ with 2D graphene to yield hybrid systems, where charge transfer processes result in the emergence of interesting optoelectronic properties. The Raman shift in the G- and 2D-modes of the hybrids relative to bare graphene, confirms that hole-doping is occurring in graphene with END1, while electron-doping occurs with END2. From our analysis we conclude that charge transfer and consequent photocurrent $I_{\rm ph}$ generation contribute to a high ${\mathcal R}$ of $\sim 10^9$ A W⁻¹ and $\sim 10^8$ A W⁻¹ in the END₁-graphene and END₂-graphene, respectively, over wavelengths λ of 400 to 1100 nm. The \mathcal{R} for END₁-graphene reported in this work is ~10 times higher compared to the MoS2-graphene heterostructure photodetectors with $\mathcal{R} \sim 10^8 \,\mathrm{A} \,\mathrm{W}^{-1}$ reported previously.

2. Results and discussion

2.1 Graphene-Sc₃N@C₈₀ hybrid

The electrophoretic deposition technique was used to deposit \sim 1 mg mL⁻¹ END₁ in *ortho*-dichlorobenzene (o-DCB) on top of the graphene membrane and the device was vacuum annealed for ~ 24 hours at ~ 180 °C (Fig. S1, ESI†). Insights into the structural morphology of END1 agglomerated on top of the

graphene membrane was obtained using Scanning Electron Microscopy (SEM) and Atomic Force Microscopy (AFM) (Fig. S2, ESI†). The influence of annealing on the optical characteristics of the device has not been evaluated presently, but will be interesting to pursue for a future study. The bare graphene thickness was ~24 nm measured using AFM indicating the presence of multi-layer graphene (MLG), as shown by the height profile scan in the inset of Fig. S2(e)-(i) (ESI†). Fig. S2(f)(i) and (ii) (ESI†) illustrate the clusters of bare END₁ in the form of islands exhibiting a peak height of ~3.6 nm and diameter ~50 nm. On the other hand, Fig. S2(g)(i)-(ii) (ESI†) reveals clustering of END₁ on the graphene surface with a peak height of \sim 9-20 nm and cluster diameter \sim 200-350 nm.

The bare END₁, bare graphene, and END₁-graphene hybrid assemblies were further characterized using Raman spectroscopy, as well as temperature T dependent Raman, which is a non-invasive characterization technique used for inferring the structural and electronic properties of materials. 42 Fig. 1(a) shows the Raman spectra of END₁-graphene hybrid at room T which is compared to bare graphene, while the inset shows the Raman spectra of the bare END₁ with a central peak at 1203 cm⁻¹ and a relative normalized peak intensity $I_{\rm END}$ ~ 1 a.u. This peak is blue-shifted $\Delta\omega^{(+)}$ by ~ 50 cm⁻¹ for the END₁-graphene Raman hybrid (with relative normalized peak intensity for $I_{\text{END}_1} \sim 0.4$ a.u., as shown) and is attributed to the van der Waals interaction between END1 and the graphene membrane.30 Fig. 1(b) and (c) show the magnified G- and 2D-bands of END₁-graphene relative to bare graphene, respectively, at room T. The $\Delta\omega^{(+)}$ shift for the G-band and 2D-band were measured to be ~ 5 cm⁻¹ and ~ 10 cm⁻¹, respectively. The $\Delta\omega^{(+)}$ shift for the G- and the 2D-band for END₁-graphene observed here is similar to the $\Delta\omega^{(+)}$ shift for the G- and the 2D-band for C₆₀-graphene hybrids reported by Jnawali *et al.* ¹⁰ The $\Delta\omega^{(+)}$ shift is attributed to C₆₀ causing p-type doping in graphene that has been confirmed using THz-time domain spectroscopy.¹⁰ Thus, from the $\Delta\omega^{(+)}$ shift for the G-band and 2D-band of END₁-graphene, it can be inferred that END₁ also induces p-doping in graphene. This assertion is in alignment with the oxidation potential of END₁ which is ~0.59 mV, measured using cyclic voltammetry, implying that END₁ is a p-type dopant.³⁹ Besides using Raman Spectroscopy to deduce doping effects, three terminal devices with back gating can also allow for the verification of doping on a future study.

The T-dependent Raman spectra of graphene and of the END₁-graphene hybrid were measured from $T \sim 298$ K to \sim 873 K and the data are plotted in Fig. 1(d). The G-band peak position experienced a red shift with temperature, where a $\Delta\omega[T]^{(-)}$ shift of $\sim 14~{\rm cm}^{-1}~(\sim 1580~{\rm cm}^{-1}~{\rm at}~T\sim~298~{\rm K}~{\rm to}$ $\sim 1566 \text{ cm}^{-1}$ at $T \sim 873 \text{ K}$) for bare graphene (bottom plot of Fig. 1(d)) was observed as T increased from \sim 298 K to \sim 873 K. A similar $\Delta\omega[T]^{(-)}$ shift of $\sim 23~{\rm cm}^{-1}$ ($\sim 1586~{\rm cm}^{-1}$ at $T\sim 298~{\rm K}$ to $\sim 1563~{\rm cm}^{-1}$ at $T\sim 873~{\rm K}$) was also observed for the END_1 -graphene hybrid (top plot of Fig. 1(d)) as T increases. The G-band shift towards lower frequencies is attributed to optical phonon softening as T increases given that the G-band is intimately associated with optical phonons which are very

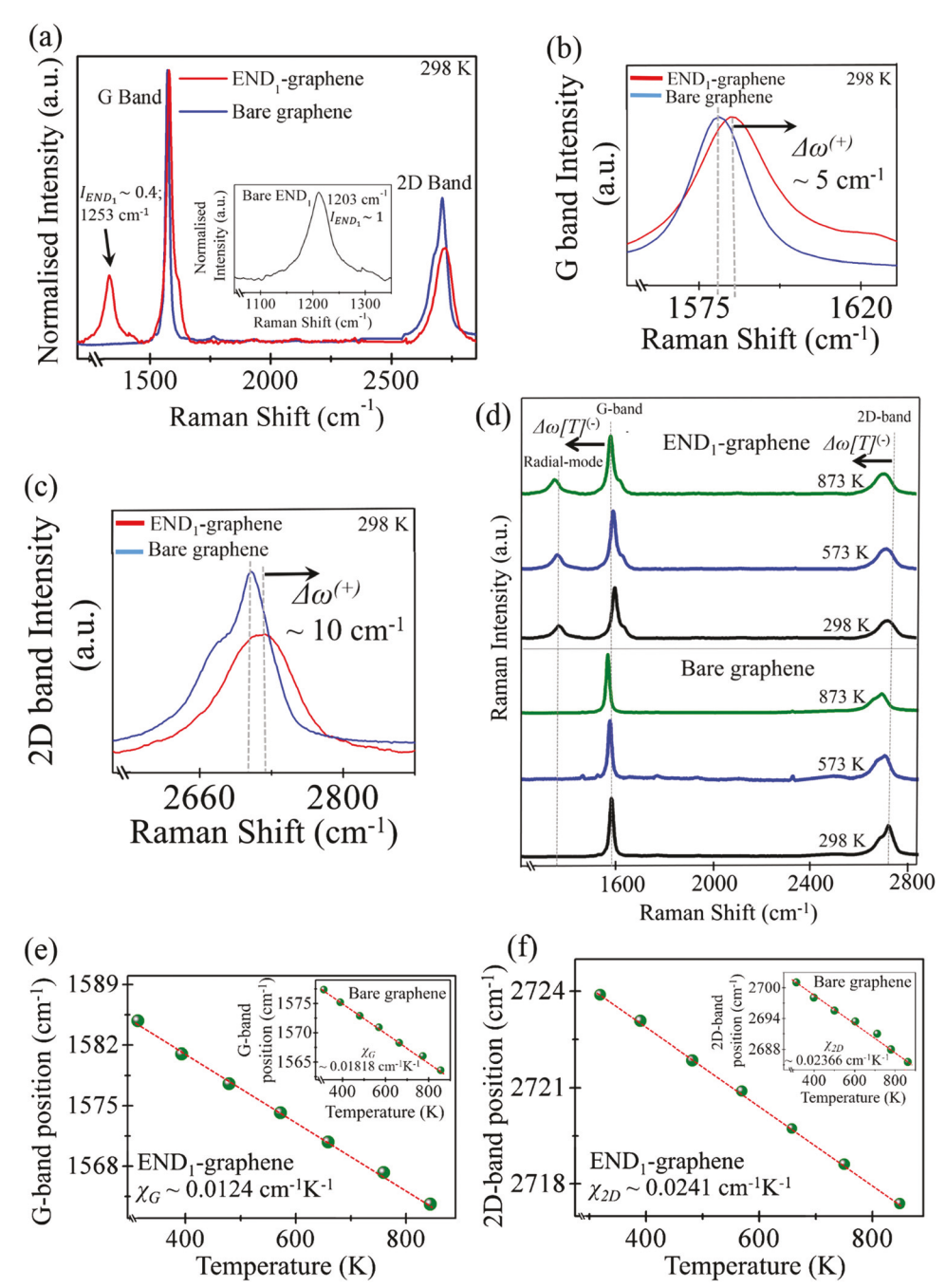


Fig. 1 (a) Raman spectra of END₁-graphene hybrid and bare graphene at room T. Inset shows the Raman spectra of the bare END₁ film. The peak at \sim 1203 cm $^{-1}$ in the inset is the tangential mode of END₁ with a relative normalized peak intensity $I_{\text{END}_1} \sim 1$ a.u. This peak is blue-shifted $\Delta \omega^{(+)}$ by \sim 50 cm⁻¹ in the END₁-graphene Raman spectra, as shown (with relative normalized peak intensity for $I_{\text{END}_1} \sim 0.4$ a.u.) and is attributed to the van der Waals interaction between the END₁ and the graphene membrane. The mechanically exfoliated graphene membranes show an intense tangential mode G-band at \sim 1580 cm⁻¹ and a 2D-band at \sim 2714 cm⁻¹. (b) and (c) are the magnified G- and 2D-band peaks, respectively, for graphene and END₁-graphene. The G-peak of graphene experiences a $\Delta\omega^{(+)}$ shift of \sim 5 cm⁻¹ and for the 2D-peak the $\Delta\omega^{(+)}$ shift is \sim 10 cm⁻¹ which is due to the p-type doping induced in graphene by END₁. (d) Variation of the G- and 2D-band with T in the END₁-graphene hybrid (top) and bare graphene (bottom). Its clear that a red-shift $\Delta\omega[T]^{(-)}$ is seen in both cases for the G- and 2D-bands as T increases. (e) Linear fit (dotted red lines) showing the extracted χ_G for the G-band, and (f) χ_{2D} for the 2D-band in END₁-graphene. Insets in (e) and (f) show the respective values for bare graphene. In this case $\chi_{G} < \chi_{2D}$ $(\sim 0.01818 \text{ cm}^{-1} \text{ K}^{-1} \lesssim 0.02366 \text{ cm}^{-1} \text{ K}^{-1} \text{ for bare graphene and } \sim 0.0124 \text{ cm}^{-1} \text{ K}^{-1} \lesssim 0.0241 \text{ cm}^{-1} \text{ K}^{-1} \text{ for END}_1 - \text{graphene})$

sensitive to carrier density.⁴³ Similarly, the 2D-band peak experiences a $\Delta\omega[T]^{(-)}$ shift of $\sim 14~{\rm cm}^{-1}$ for bare graphene $(\sim 2701 \text{ cm}^{-1} \text{ at } T \sim 298 \text{ K to } \sim 2683 \text{ cm}^{-1} \text{ at } T \sim 873 \text{ K})$ (bottom of Fig. 1(d)), and the END₁-graphene hybrid also

underwent a $\Delta\omega[T]^{(-)}$ shift of ~ 16 cm⁻¹ (~ 2714 cm⁻¹ at $T \sim 298 \text{ K to } \sim 2698 \text{ cm}^{-1} \text{ at } T \sim 873 \text{ K}) \text{ (top plot of }$ Fig. 1(d)). Incidentally, the 2D-band is sensitive to changes in the electronic band structure such as that arising from strain,

Communication

which in this case would imply temperature-induced strain changes for the bare graphene and for the END_1 -graphene hybrid.⁴⁴

The Raman shifts of the G-band and 2D-band as a function Twere further analysed by extracting the fitting parameters when the data are fit to $\omega = \omega_0 + \chi T$; here ω_0 is the extrapolated peak position at 0 K, and γ is the first-order T-coefficient. From the linear fit for the G-band and the 2D-band for END1graphene shown in Fig. 1(e) and (f), respectively, the firstorder T coefficients for bare graphene were calculated to be $\chi_{\rm G} \sim 0.01818~{\rm cm}^{-1}~{\rm K}^{-1}$ and $\chi_{\rm 2D} \sim 0.02366~{\rm cm}^{-1}~{\rm K}^{-1}$ (insets in Fig. 1(e) and (f)). Equivalently, the T-coefficients for the END_1 -graphene hybrid were $\chi_G \sim 0.0124~cm^{-1}~K^{-1}$ and $\chi_{\rm 2D} \sim 0.0241~{\rm cm}^{-1}~{\rm K}^{-1}$. In our case $\chi_{\rm G} < \chi_{\rm 2D}$ $(\sim 0.01818~{\rm cm}^{-1}~{\rm K}^{-1} \lesssim 0.02366~{\rm cm}^{-1}~{\rm K}^{-1}$ for graphene, and $\sim 0.0124 \text{ cm}^{-1} \text{ K}^{-1} \lesssim 0.0241 \text{ cm}^{-1} \text{ K}^{-1} \text{ for END}_1\text{-graphene}$ which is consistent with a previous report by Tian et al. 43 who determined $\chi_G \sim 0.01496~\text{cm}^{-1}~\text{K}^{-1} < \chi_{2D} \sim 0.02484~\text{cm}^{-1}~\text{K}^{-1}$ for graphene, and explained this result on the basis of the "selfenergy" contribution from the G-band.

The I-V measurements of the END₁–graphene hybrid were conducted in a vacuum probe stage at a pressure of $\sim 10^{-6}$ Torr, where T was controlled from ~ 5.8 K to 298 K using a closed-cycle He refrigerator and the results were compared to those of bare END₁ and bare graphene, as shown in Fig. 2(a). At $T \sim 298$ K, the

transport current I is ~ 20 times higher for END₁-graphene relative to bare graphene and bare END1, as the data in Fig. 2(a) reveal. In Fig. 2(b), the I increased from \sim 12 mA at $T \sim 5.8$ K to ~ 24 mA at $T \sim 298$ K for $V \sim 1$ V for the END₁-graphene hybrid, while in Fig. 2(c), the I increases from ~ 0.38 mA at $T \sim 5.8$ K to ~ 0.8 mA at $T \sim 298$ K for bare graphene at $V \sim 1$ V. Similarly, in the inset of Fig. 2(c) for bare END₁, I increases from ~ 0.5 mA at $T \sim 5.8$ K to ~ 2.1 mA at $T \sim 298$ K. These data clearly show that the device resistance R for the bare END₁, bare graphene, and END₁-graphene hybrid decreases as T increases and that the adsorption of END₁ results in modulation of the electronic transport in graphene. The dependence of R with T is further delineated by the data in Fig. 2(d), where the inset shows the R-T Characteristic of bare graphene, bare END₁ and the END₁-graphene hybrid. An inverse correlation of R with T is evident for all three cases, as shown in the inset of Fig. 2(d) with some nonlinearities present. Defects in bare graphene may be responsible for the inverse T-dependence of R which has been previously reported, 45 and in the case of END₁-graphene may also arise from the p-type doping induced. 46 Additionally, for bare END₁ as T increases, the charge carriers in END₁ have a higher likelihood of overcoming the potential barrier and thus decreasing R.33 Liu et al.47 used the Efros-Shklovskii model to calculate the activation energy E_a of

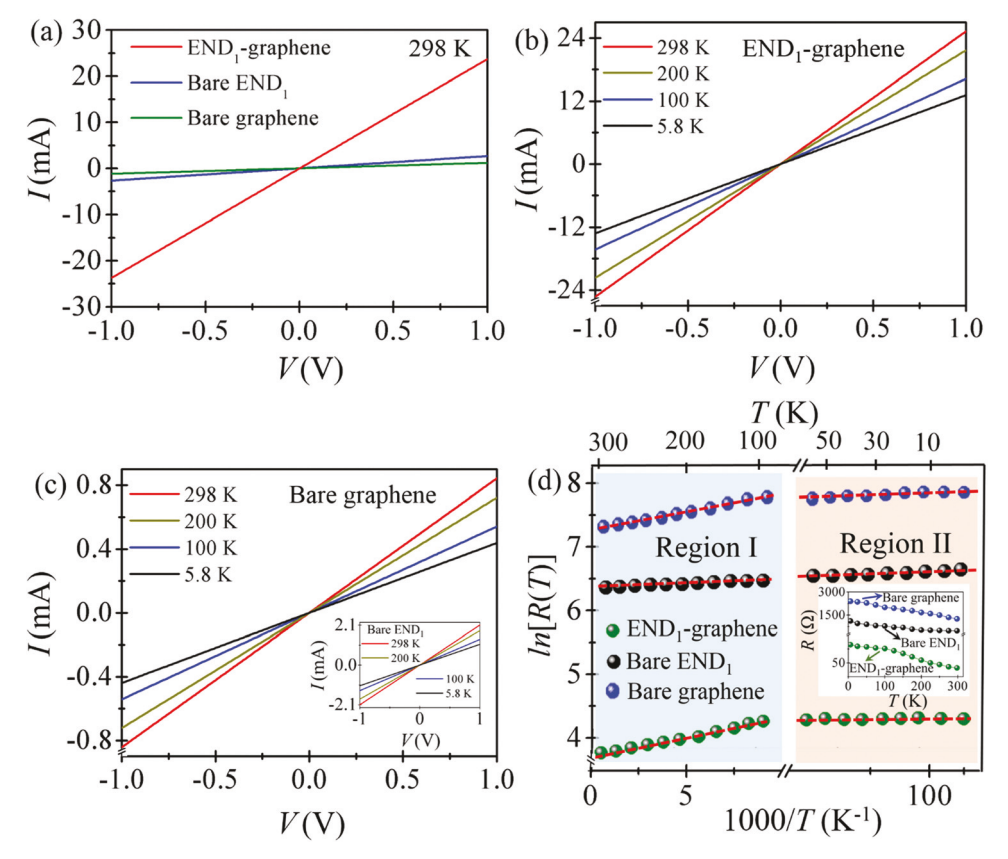


Fig. 2 The I-V of (a) END₁-graphene, bare END₁, and bare graphene at $T\sim298$ K. The I-V of (b) END₁-graphene, (c) bare graphene, and END₁ (inset) over various temperatures. (d) Logarithmic plot of $\ln[R(T)]$ as a function of 1000/T. Two regions were used to plot $\ln[R(T)]$ as a function of 1000/T, namely Region I (65–298 K) and Region II (5.8–60 K), showing the linear fit of the data (solid red lines). The inset shows a non-linear R versus T plot for bare graphene, bare END₁, and END₁-graphene. The E_a values were extracted from this fit and the results are summarized in Table 2.

few-layer graphene interconnects, but the fit encompassed significant uncertainty for T from ~ 5 –340 K. Therefore, in our analysis we consider two distinct regions shown in Fig. 2(d) from $T \sim 65$ –298 K (Region I), and from $T \sim 5.8$ –60 K (Region II), where the data are fit to the Arrhenius model⁴⁸ denoted by eqn (1) below,

$$R(T) = R_0 \exp\left[\frac{E_a}{2kT}\right] \tag{1}$$

Here R(T) is the resistance at T, R_0 is the resistance at $T = \infty$ and is referred to as the pre-exponent, E_a is the thermal activation energy, and k is the Boltzmann constant. Eqn (1) is rewritten as,

$$\ln R = \ln R_0 + \frac{E_a}{2kT} \tag{2}$$

where a linear relationship is expected between the ln[R(T)] versus T plot. As noted, two regions were used to plot ln[R(T)] as a function of 1000/T, shown in Fig. 2(d) where E_a is deduced from the slope of this fit. Table 1 summarizes the E_a values tabulated for Region I (\sim 65–298 K) and Region II (\sim 5.8–60 K), along with the r^2 values where r is the correlation coefficient, for bare graphene, bare END₁, and the END₁-graphene hybrid. For Region I, E_a was tabulated to be ~ 0.73 meV for bare graphene, ~ 0.54 meV for bare END₁, and ~0.43 meV for END₁-graphene. Similarly, for Region II, $E_{\rm a} \sim 0.94$ meV for bare graphene, ~ 0.76 meV for bare END₁, and ~ 0.61 meV for END₁-graphene were determined. We believe the physical origin of the different activation energies comes from two mechanisms that maybe operative. The first is likely due to a thermally activated hopping mechanism related to defects in the underlying graphene, which is dominant at the lower temperatures (Region II) with the larger activation energies. The defects in the underlying graphene in our END₁-Graphene hybrid are likely to contribute to Region II's larger activation energy, and hence larger resistance, where dopants maybe largely frozen out. In the higher temperature regime (Region I), the dopants have a higher likelihood for getting activated due to increased thermal energies which would result in an increase in charge carrier density, conductivity, reduced resistance and hence lower activation energy, as noted in Table 1 by the activation energy values we have tabulated. The E_a values for the hybrid structures are lower by \sim 41% and \sim 35% for both Region I and Region II, respectively, when compared to bare graphene. This reduction in E_a is consistent with the p-type doping induced in graphene as a result of interactions with END₁, and is also inferred from the $\Delta\omega[T]^{(-)}$ shift of the Raman spectrum (Fig. 1(a)).

Table 1 The activation energy $E_{\rm a}$ and correlation coefficient r^2 fitting values for bare graphene, bare END₁, and END₁–graphene hybrid for Region I (\sim 65–298 K) and Region II (\sim 5.8–60 K). The $E_{\rm a}$ was lowest for the END₁–graphene hybrid

| | Region I (6 | 5-298 K) | Region II (5.8-60 K) | |
|----------------------------|-------------------|--------------|----------------------|--------------|
| Device | $E_{\rm a}$ (meV) | r^2 | $E_{\rm a}$ (meV) | r^2 |
| Bare graphene | ~0.73 | ~0.915 | ~0.94 | ~ 0.994 |
| Bare END ₁ | ~ 0.54 | ~ 0.918 | ~ 0.76 | ~ 0.992 |
| END ₁ -graphene | ~ 0.43 | ~ 0.925 | ~ 0.61 | ~0.993 |

The END₁-graphene and bare END₁ devices were exposed to a white light source to initiate the optoelectronic transport measurements of these devices under vacuum. The $I_{\rm ph}$ was extracted from the measurements done in the dark (i.e. I_{dark}) and in the presence of light (i.e. I_{light}) where $I_{ph} = I_{light} - I_{dark}$. Under illumination, as shown in Fig. 3(a), the I_{light} values were \sim 10 times higher for the hybrid (\sim 25.15 mA at 0.5 V) compared to the bare END₁ (inset) where $I_{\rm light} \sim 2.5$ mA at 0.5 V at room T. We note here that our devices are based on a twoterminal device architecture where the photoconductive mechanism (no gate voltage applied) is operative, unlike in prior work^{8,12,24,49-51} that relied on an external gate voltage applied, based on a three-terminal device architecture. Fig. 3(b) shows the time-dependent I_{ph} measurements of bare END₁, bare graphene, and the END₁-graphene hybrid at ~ 1 V (where $I_{
m light} \sim 26.43$ mA and $I_{
m dark} \sim 25.20$ mA for END₁–graphene, and $I_{\rm light} \sim 2.82$ mA and $I_{\rm dark} \sim 2.07$ mA for END₁). The cycles in yellow refer to the ON-state of the light pulses, while the OFF-cycles (no color) represent the absence of light. A photoresponse was not detectable in our bare graphene device, as the $I_{\rm ph}$ was below the pico-amp range (secondary y-axis). As reported earlier, in graphene, a short photon-generated carrier lifetime persists on the scale of picoseconds, and the ON/OFF ratio is also quite poor.8 Fig. 3(c) shows the response of the photocurrent over a single ON-pulse, where the rise time τ_r and decay time τ_d for bare END₁ and END₁-graphene are measured. The τ_r and τ_d are among the figures of merit that are important to gauge the photodetector response. The τ_r is measured from \sim 10% of the noise floor and \sim 90% of the peak signal value. Similarly, τ_d was computed from $\sim 90\%$ to 10% of the maximum and minimum signal intensities, respectively.⁵² These values were $\tau_{\rm r} \sim 1.8$ ms and $\tau_{\rm d} \sim 2.7$ ms for the END₁-graphene hybrid, and for bare END₁, $\tau_r \sim 2.6$ ms and $\tau_d \sim 3.1$ ms. The response time for our END₁-graphene hybrid is significantly lower compared to PbS QDs-graphene hybrids ($\tau_{\rm r} \sim 10$ ms and $\tau_{\rm d} \sim 20 \text{ ms})^{49}$ and Bi₂Te₃-graphene hybrids $(\tau_{\rm r} \sim 8.7 \text{ ms})^{51}$ as photodetectors reported previously.

The \mathcal{R} for END₁-graphene and bare END₁ was calculated using $\mathscr{R} = \frac{I_{\mathrm{ph}}}{P}$, where P is the incoming power, and the values were determined to be $\sim\!4\times10^9~A~W^{-1}$ and $2\times10^8~A~W^{-1}$ at \sim 1 V and $P \sim 3.3$ pW at room T, respectively, with an incoming light power density (calibrated using the Thorlabs optical power meter PM100D) ~ 3 mW cm⁻². Fig. 3(d) shows the band diagram illustrating the charge transport between the END₁graphene interface at equilibrium (top of Fig. 3(d)) and upon illumination (bottom of Fig. 3(d)). The lowest unoccupied molecular orbital energy (LUMO) of END₁ is ~ -4.6 eV, while the HOMO level is ~ -5.7 eV.⁵³ Upon illumination, the incident photons excite ground-state electrons of END₁ into excited states. Electron-hole pairs are then formed at the END₁-graphene interface and photogenerated holes are efficiently injected into the graphene; thus, END₁ is a p-type dopant with graphene which is also consistent with the high oxidation potential of END₁ ~ 0.59 mV.³⁹ This leads to an increase in the hole carrier density as the hole population in graphene

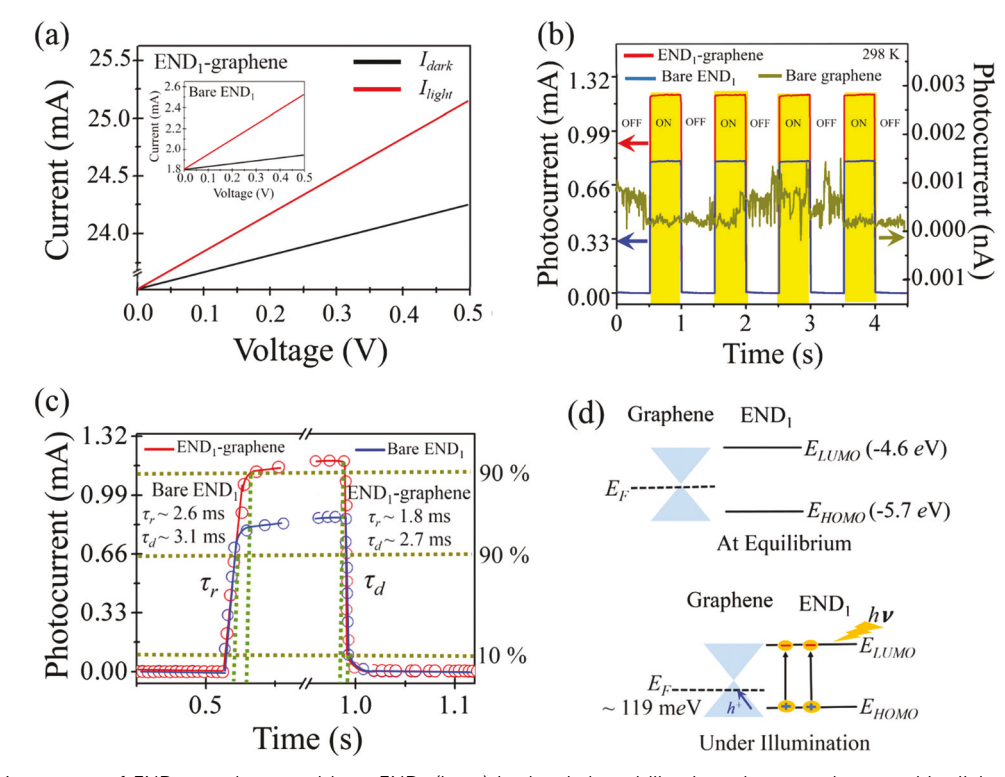


Fig. 3 (a) The I-V response of END₁-graphene and bare END₁ (inset) in the dark and illuminated states where a white light source was used for illumination in vacuum at room T. (b) The $I_{\rm ph}$ was extracted from the measurements done in the absence and presence of light over multiple ON (yellow) and OFF (no color) cycles (where, $l_{light} \sim 26.43$ mA and $l_{dark} \sim 25.20$ mA for END₁–graphene, and $l_{light} \sim 2.82$ mA and $l_{dark} \sim 2.07$ mA for END₁) at ~ 1 V. The bare graphene device yields a nondiscernable photoresponse, as shown by the secondary y-axis. (c) A magnified single ON-cycle pulse, where the τ_r and τ_d were calculated. Left and right insets list the values of τ_r and τ_d for bare END₁-graphene, respectively. (d) Schematic representation of the band diagram for graphene and END_1 at equilibrium (top) and under illumination (bottom) illustrating the hole transfer from END_1 to graphene. The $E_{\rm F}$ of graphene experiences a downward shift by ~119 meV.

increases, 10 as shown schematically in Fig. 3(d). The injection of holes leads to the downward shift in $E_{\rm E}$ in graphene, ⁵⁴ and to electron injection into END1, where charge neutrality is maintained in the hybrid. Flores et al. reported that hole-doping in exfoliated graphene using various process treatments shifts $E_{\rm F}$, and $E_{\rm F}$ and carrier concentration (N) at room T are determined from the shift in the Raman peak positions using eqn (3) and (4) below, 55

$$E_{\rm F} ({\rm eV}) = \left| \frac{{\rm Position}({\rm G\text{-}band}) - 1580}{42} \right| \tag{3}$$

$$N \text{ (cm}^{-2}) = \frac{\left(\frac{E_{\rm F}}{\hbar \nu_{\rm F}}\right)^2}{\pi} \tag{4}$$

Position (G-band) refers to the peak position of the G-band which occurs at 1585 cm⁻¹ for the hybrid (from Fig. 1(b)), $\nu_{\rm E}$ = $1.09 \times 10^6 \text{ m s}^{-1}$ is the Fermi velocity and \hbar is the modified Planck's constant (i.e. $\hbar = h/2\pi$, where $h = 6.626 \times 10^{-34}$ J s). From our Raman data in Fig. 1(b), we calculated a value for $E_{\rm F} \sim 119$ meV and accordingly $N \sim 8.5 \times 10^{11}~{\rm cm}^{-2}$ at ~298 K. The results are also consistent with the observed $\Delta\omega^{(+)}$ shift for the G-band in Fig. 1(b), which is attributed to holedoping in graphene, and in turn induces the downward shift in $E_{\rm F}$ in graphene.⁵⁶

To further explore the photodetector response, a tunable laser source, the Fianium LLFT Contrast (NKT Photonics), was used for optical excitation, and wavelength λ was increased in \sim 100 nm increments from 400–1100 nm. Fig. 4(a)–(d) show the comparative evaluation of I_{ph} , \mathcal{R} , detectivity D, and external quantum efficiency EQE of the END₁-graphene hybrid and bare END₁ (insets) as a function of λ over T ranging from ~ 5.8 K to 298 K. The $I_{\rm ph}$ and \mathcal{R} for END₁-graphene hybrids were found to be ~ 0.6 mA and just below $\sim 5 \times 10^9$ A W⁻¹ at $\lambda \sim 400$ nm, while the bare END₁ devices (insets of Fig. 4(a) and (b)) show an $I_{\rm ph} \sim 0.12$ mA and $\mathscr{R} \sim 2 \times 10^8$ A W⁻¹, respectively. A decrease in both parameters is seen for $\lambda \gtrsim 850$ nm over the temperatures tested. Moreover, D and EQE in Fig. 4(c) and (d) were

calculated using
$$D$$
 (Jones) = $\frac{\sqrt{A}}{\sqrt{2 \cdot e \cdot I_{\text{dark}}}} \mathcal{R}$, where $I_{\text{dark}} = \frac{h_c}{\sqrt{2 \cdot e \cdot I_{\text{dark}}}} \mathcal{R}$

25.2 mA, $A = 708.46 \ \mu\text{m}^2$ and EQE (%) = $\frac{hc}{e \cdot \lambda} \mathcal{R}$, where $e = 1.6 \times 10^{-19}$ C is the electronic charge. The D and EQE of END₁-graphene hybrids were calculated to be $\sim 9.6 \times$ 10^{15} Jones and $\sim 10^9$ % at $T \sim 298$ K, respectively, as shown in Fig. 4(c) and (d), respectively. The D and EQE of the bare END₁ (insets of Fig. 4(c) and (d)) were measured to be $\sim 10^{12}$ Jones and $\sim 10^6$ % at $T \sim 298$ K at $\lambda \sim 400$ nm. Again, both parameters decrease for $\lambda \gtrsim 850$ nm over the temperatures tested. It is notable that END1 and END1-graphene show an

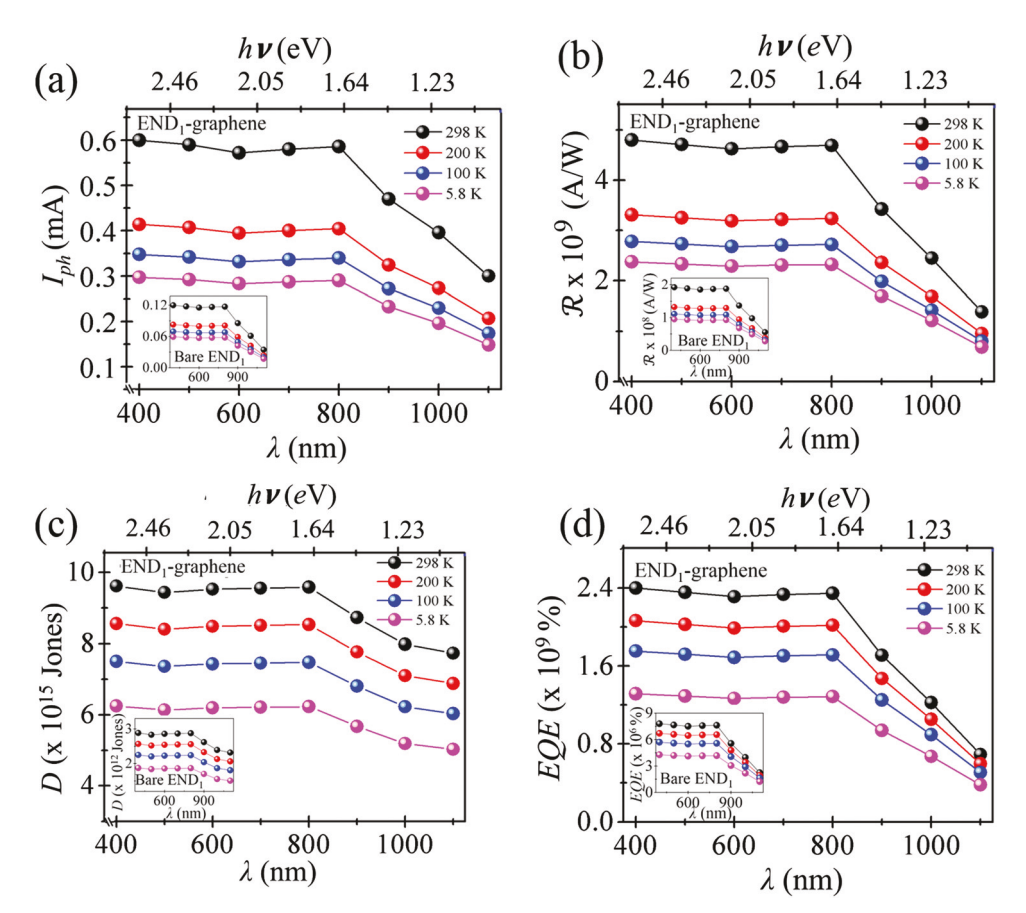


Fig. 4 (a)–(d) Comparative analysis of the T-dependent I_{ph} , \mathcal{R} , D, and EQE of END_1 –graphene, and bare END_1 (insets) from $\lambda \sim 400$ –1100 nm at various T. (a) For $\lambda \sim 400$ nm, the device shows high $I_{\rm ph}$ (~ 0.6 mA) and (b) high \Re (approaching 5×10^9 A W⁻¹) for END₁-graphene at $T \sim 298$ K and $I_{\rm ph}$ and \mathscr{R} start to decrease for $\lambda \gtrsim 850$ nm. This decrease is due to the fact that an efficient photoconductance appears in the END₁ film at $h\nu \gtrsim 1.64$ eV (i.e. $\lambda \gtrsim 850$ nm). The (c) D and (d) EQE of END₁-graphene hybrids were calculated to be $\sim 9.6 \times 10^{15}$ Jones and $\sim 10^9$ % at ~ 298 K at $\lambda \sim 400$ nm, respectively. A similar trend was observed for the bare END₁ (insets of (a)-(d)) from $\lambda \sim 400-800$ nm. At $\lambda \sim 400$ nm, the $I_{\rm ph}$ and \Re for bare END₁ were \sim 0.12 mA and \sim 2 \times 10 8 A W $^{-1}$, and D and EQE for END₁ were \sim 2.8 \times 10 12 Jones and \sim 10 6 % at $T\sim$ 298 K.

increase in photoresponse for $h\nu \gtrsim 1.64$ eV (i.e. $\lambda \leq 850$ nm), which demonstrates that the photoinduced carriers are only generated for λ below this value, where the carriers have sufficient energy to overcome the energy barrier. The values of $I_{\rm ph}$, \mathcal{R} , D, and EQE are indeed enhanced significantly through the interaction of END₁ with graphene compared to the bare END₁ system. Additionally, the D and EQE are comparable to the previously reported values for graphene-perovskite (MAPbI₃) devices ($D \sim 10^{15}$ Jones and EQE $\sim 10^8$ %).⁵⁰

2.2 Graphene-La@C₈₂ hybrid

To delve further into the graphene-endohedral hybrid interaction, we conducted experiments with another endohedral fullerene, La@C82 denoted as END2 here, that was deposited on top of the graphene. The same methodology was used to deposit END2, as discussed in Section 2.1 for END1. Before the preparation of the END2-graphene hybrid devices, initial measurements were conducted on the bare END2 as shown by the electrophoretic deposition data depicted for END2 in Fig. S3, ESI† and to also measure the intrinsic conductance of these endohedrals. Further, AFM was used to determine the agglomeration of END₂ on top of the graphene membrane (Fig. S4, ESI†). The bare graphene thickness was ~ 12.8 nm measured using AFM indicating MLG. The cluster arrangement for END₂ on graphene is seen in Fig. S4(b)(i) and (ii) (ESI†).

The END₂-graphene hybrid was further characterized using Raman Spectroscopy, where Fig. 5(a) shows the Raman spectra of the END_2 -graphene hybrid and the bare graphene at room T; the inset in Fig. 5(a) shows the Raman spectra of the bare END₂ film. The peaks at $\sim 672 \text{ cm}^{-1}$, $\sim 692 \text{ cm}^{-1}$, $\sim 753 \text{ cm}^{-1}$, and \sim 792 cm⁻¹ in the inset represent the intrinsic internal vibrational modes of END2. 39 The G-peak of graphene experiences a $\Delta\omega^{(-)}$ shift of $\sim 6 \text{ cm}^{-1}$ (from $\sim 1580 \text{ cm}^{-1}$ to $\sim 1574 \text{ cm}^{-1}$) as shown in the magnified plot of Fig. 5(b), while the 2D-peak undergoes a $\Delta\omega^{(-)}$ shift of $\sim 12~{\rm cm}^{-1}$ (from $\sim 2704~{\rm cm}^{-1}$ to \sim 2692 cm⁻¹) illustrated in Fig. 5(c). In the END₂-graphene hybrid, a peak at \sim 789 cm⁻¹ (with relative normalized peak intensity for $I_{\text{END}_2} \sim 0.04$ a.u.) is seen, which for the bare END₂ film occurs at 792 cm⁻¹. This shift arises from the van der Waals interaction between END2 and graphene. The La atom has three valence electrons in its outermost shell and has a strong tendency to donate electrons. 40 Also, from the Raman red shift of $\Delta\omega^{(-)}$ for the G- and the 2D-band, we infer that END₂ induces n-type doping in graphene, which is in alignment

Communication

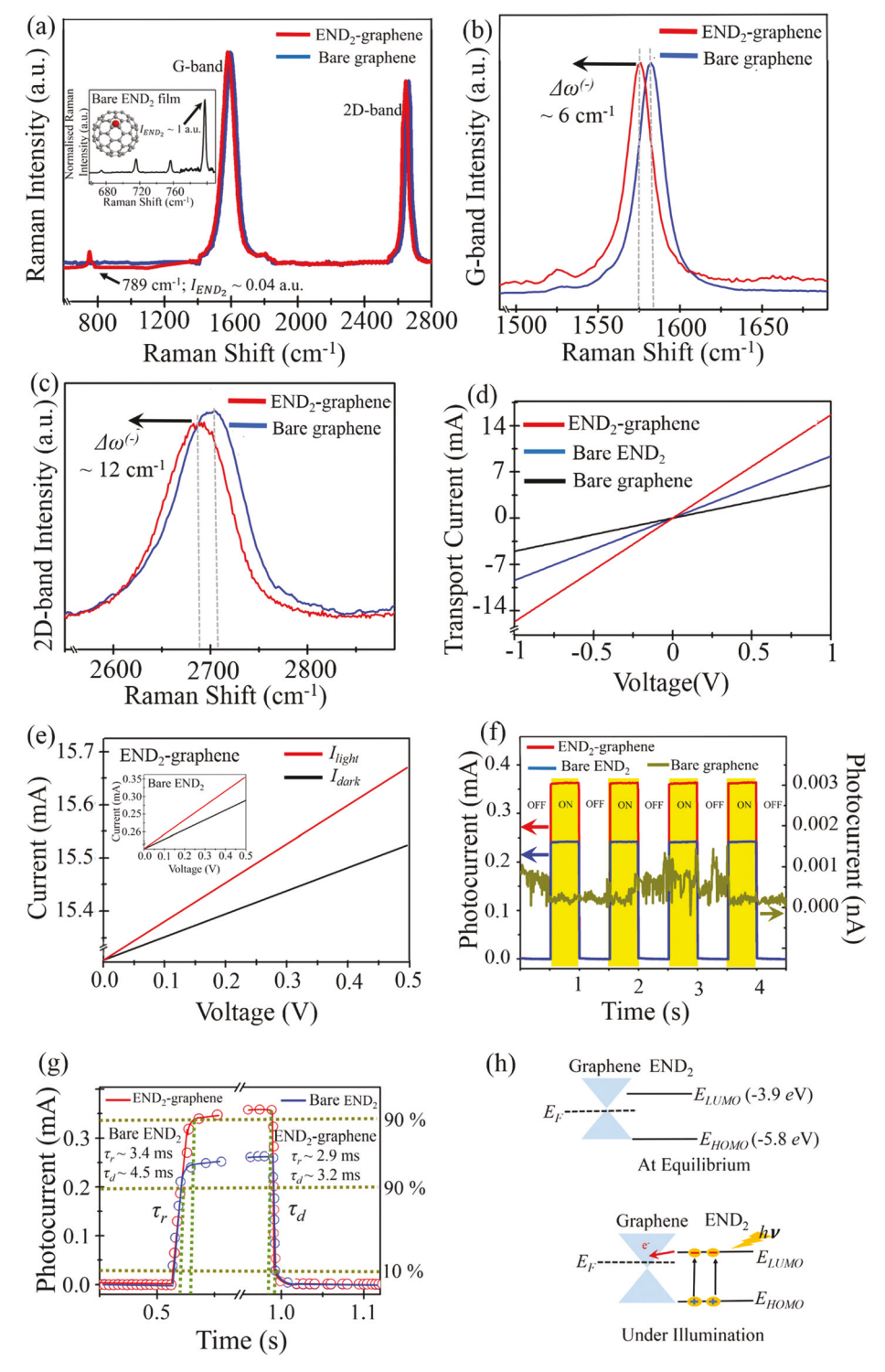


Fig. 5 (a) Raman spectra of END₂-graphene and bare graphene. Inset shows the Raman spectrum for the bare END₂ film. The peaks at \sim 672, 692, 753, and 792 cm⁻¹ represent the internal vibrational modes of END₂. In the END₂-graphene hybrid, the main 792 cm⁻¹ peak for END₂ shifts to \sim 789 cm⁻¹ and is attributed to the van der Waals interaction between END₂ and graphene. (b) The G-band of graphene experiences a $\Delta\omega^{(-)}$ shift of \sim 6 cm $^{-1}$ and (c) the 2D-band red-shifts by \sim 12 cm $^{-1}$. From the $\Delta\omega^{(-)}$ shift for the G- and the 2D-band it can be inferred that END₂ induces n-type doping in graphene. (d) The I-V Characteristics of the END2-graphene hybrid, bare END2, and bare graphene where transport is enhanced for the END2-graphene hybrid device. (e) The I-V of the END₂-graphene hybrid and bare END₂ (inset) in the dark and illuminated states for a white light source at room T. (f) Pulsed ON (yellow) and OFF (no color) cycles showing the photoresponse for the three cases at 1 V bias (where, $I_{light} \sim 16.15$ mA and $I_{dark} \sim 15.80$ mA for END₂–graphene, and $l_{\text{light}} \sim 0.61$ mA and $l_{\text{dark}} \sim 0.38$ mA for END₂). (g) A magnified single ON-cycle pulse, where the τ_r and τ_d were calculated. Left and right insets show the values of τ_r and τ_d for bare END₂ and END₂-graphene hybrid, respectively. (h) Schematic representation of the energy band diagram for graphene and END2 at equilibrium (top), and under illumination (bottom) illustrating the electron transfer from END2 to graphene, inducing the n-type character in graphene.

with the oxidation potential for $\ensuremath{\text{END}}_2$ that is discussed in more detail below.

Electrical measurements of the END2-graphene hybrid were compared to bare graphene and bare END_2 at room T, as shown in Fig. 5(d). The $I_{\rm dark}$ values were twice as high for the END₂graphene hybrid relative to bare END2. The hybrid also shows enhancement in optoelectronic transport properties when illuminated with a white light source as shown by the data in Fig. 5(e). The time-dependent I_{ph} of the END₂-graphene hybrid was also measured as shown in Fig. 5(f) for 1 V bias, and the results were compared with bare graphene and the bare END₂. The END₂-graphene hybrid exhibited the highest I_{ph} , while a negligible photoresponse resulted from the bare graphene device (secondary axis of Fig. 5(f)); here $I_{\text{light}} \sim 16.15 \text{ mA}$ and $I_{\rm dark} \sim 15.80$ mA for END₂-graphene at 1 V, and $I_{\rm light} \sim$ 0.61 mA and $I_{\rm dark} \sim 0.38$ mA for END₂ at ~ 1 V. Also, $\tau_{\rm r}$ and τ_d of END₂-graphene were measured in a similar fashion as for END₁, where $\tau_{\rm r} \sim 2.9$ ms and $\tau_{\rm d} \sim 3.2$ ms for the END₂graphene hybrid, and $\tau_{\rm r} \sim 3.4$ ms and $\tau_{\rm d} \sim 4.5$ ms for bare END2, as illustrated in Fig. 5(g). The R values of the END2-graphene hybrid and bare END2 were measured to be $\sim 2.8 \times 10^8 \,\mathrm{A\,W}^{-1}$ and $\sim 6 \times 10^7 \,\mathrm{A\,W}^{-1}$, respectively, at room T. The band diagram was also postulated to explain the behaviour of the hybrid at equilibrium and under illumination, as shown

schematically in Fig. 5(h) at equilibrium (top) and under illumination (bottom). Upon illumination, light is absorbed by END₂ and photo-generated carriers are created. Since a La atom has three valence electrons present in its shell and donates its electrons to the carbon cage, the LUMO level of END2 is lowered to ~ -3.9 eV compared to END₁. Thus, due to the electron-donating nature of La, n-type doping of graphene is observed.⁵⁸ Moreover, the oxidation potential of END₂ is found to be ~ 0.07 mV, ⁴⁰ and given its low value, this again implies that END₂ is a relatively good electron-donor, which is also consistent with the Raman shift (red-shifted) observed in Fig. 5(b) and (c) for n-type doping in graphene. Doping effects can also be verified through back gating measurements on a future study. Since La@C₈₂ induces n-doping in graphene, eqn (3) (applied for p-type doping in graphene)55 is not applicable in order to calculate the magnitude of the $E_{\rm F}$ shift.

Similar to the measurements conducted using END₁, the END₂–graphene hybrid device was further exposed to a wide range of λ 's from \sim 400–1100 nm using a tunable laser source, as shown by the data for $I_{\rm ph}$, \mathcal{R} , D, and EQE, in Fig. 6(a)–(d), respectively. The $I_{\rm ph}$, in Fig. 6(a) was indeed higher for the END₂–graphene hybrid device compared to bare END₂, and an \mathcal{R} of \sim 10⁸ A W⁻¹ was measured for the END₂–graphene hybrid compared to \sim 10⁷ A W⁻¹ for bare END₂, as shown in Fig. 6(b).

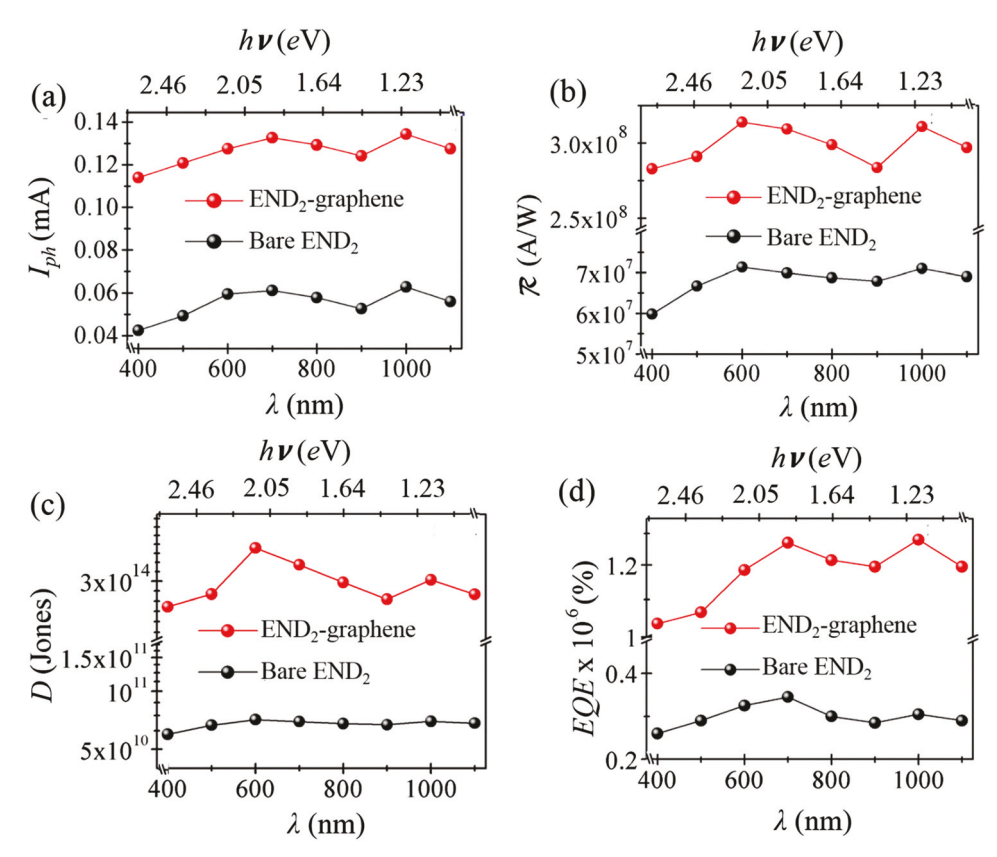


Fig. 6 The (a) I_{ph} , (b) \mathscr{R} , (c) D, and (d) EQE of the END₂–graphene hybrid and the bare END₂ from $\lambda \sim 400-1100$ nm at room T. The devices were photo responsive with $\mathscr{R} \sim 10^8$ A W⁻¹ for the END₂–graphene hybrid and $\sim 10^7$ A W⁻¹ for END₂. The promising broadband optical absorption response with END₂ is attributed to the fact that END₂ shows broad absorption bands over the entire visible and near-IR regime. From the data in (c) and (d), the D and EQE of the hybrid device was found to be $\sim 10^{14}$ Jones and $\sim 10^6$ %, respectively.

From the figures of merit. it is clear that the results reported here show the END, and END, graphene based reports for graphene hybrid structures. Table 2

Communication

| Material | Detector type | λ (nm) | $	au_{\mathrm{r}} \ \mathrm{(ms)}$ | $	au_{\mathrm{d}} \left(\mathrm{ms} \right)$ | $\mathscr{R}\left(A\;W^{-1}\right)$ | $\tau_{\rm r}$ (ms) $\tau_{\rm d}$ (ms) \mathscr{R} (A W ⁻¹) Power density (mW cm ⁻²) D (Jones), EQE (%) | D (Jones), EQE (%) | Ref. |
|--|-------------------------------|------------------|------------------------------------|---|-------------------------------------|--|--|-----------|
| Pbs QDs-SLG | Photo-gating | $\sim 400-700$ | ~ 10 | ~ 20 | $\sim 10^7$ | ~ 0.2 | $D \sim 10^{13}$ | 49 |
| Bi ₂ Te ₃ -SLG heterostructure | Photo-gating | 086∼ | ~ 8.7 | | \sim 35 | 1 | 1 | 51 |
| | Photo-gating | \sim 635 | | | $\sim\!10^8$ | $\sim\!6.4\times10^4$ | 1 | 8 |
| C_{60} -SLG | Photo-gating | ~ 200 | | | $\sim\!10^7$ | ~5 | $	ext{EQE} \sim 10^8$ | 12 |
| FeCl ₃ -FLG | Photo-conductive | ~ 375 | 1 | 1 | ~ 10 | \sim 15.3 | $D\sim 10^3$ | 25 |
| Fluorographene (fluorinated MLG) | Photo-gating/photo-conductive | $\sim 255-4290$ | ~ 80 | $\sim\!200$ | $\sim\!10^3$ | ~ 0.2 | $D \sim 10^{11}$ | 24 |
| Few layer MoS ₂ -glassy-graphene | Photo-conductive | ~ 532 | | | ~ 0.012 | 1 | $D \sim 10^{10}$ | 20 |
| MAPbI ₃ -graphene | Photo-gating | $\sim 450 – 750$ | | 628 ∼ | $\sim 10^7$ | \sim 15.4 | $D \sim 10^{15}, { m EQE} \sim 10^{8}$ | 50 |
| END ₁ -MLG | Photo-conductive | ~ 400 –1100 | $\sim\!1.8$ | \sim 2.7 | $\sim\!10^{9}$ | ~3 | $D\sim 10^{15}, \mathrm{EQE}\sim 10^9$ | This work |
| $\mathrm{END}_2	ext{-MLG}$ | Photo-conductive | ~ 400 –1100 | $\sim\!2.9$ | $\sim\!3.2$ | $\sim\!10^8$ | ~3 | $D\sim10^{14},\mathrm{EQE}\sim10^8$ | This work |

What is distinctly clear from the data in Fig. 6 is the broad absorption occurring for the END₂-graphene hybrid over the entire \sim 400-1100 spectral range, which is in contrast to the data obtained for the END₁-graphene hybrid, where absorption decreased for $\lambda \gtrsim 850$ nm. This is due to the fact that END₂ shows broad absorption bands over the entire visible and near-IR regions, which was another unique reason for us to study the dynamics of this particular endohedral with graphene in a device platform.⁵⁹

The D and EQE of the END_2 -graphene hybrid device were calculated to be $\sim 10^{14}$ Jones and $\sim 10^6$ %, respectively. We have compared our results with other graphene-based hybrid materials, 8,49-51 as shown in Fig. 6(c) and (d), and summarized in Table 2. It should be noted that the best $\mathcal{R} \sim 10^9 \, \mathrm{A \, W}^{-1}$ reported here for END₁-graphene fabricated in this study is ~ 10 times higher compared to previous MoS₂-graphene based photodetector⁸ where an $\mathcal{R} \sim 10^8 \, \text{A W}^{-1}$ was reported for $\lambda \sim 400$ –1100 nm. Our work clearly sets the stage for opening up avenues for a new class of endohedral-fullerene doped 2D-graphene hybrids to enable high performance optoelectronic devices in the future.

3. Conclusion

In summary, in this work photodetectors based on grapheneendohedral fullerenes were fabricated and characterized. From the Raman spectra analyses, confirmation of charge transfer processes occurring between the endohedral fullerenes and graphene is evident. The $\Delta\omega^{(+)}$ shift for the case of the END₁-graphene hybrid and $\Delta\omega^{(-)}$ shift in the END₂-graphene hybrid confirms that graphene acts as an electron donor in the former case, and as an electron acceptor in the latter case. Both END₁-graphene and END₂graphene hybrid devices display a strong photoresponse under optical illumination. The photoinduced free holes (or electrons) are injected into graphene with END₁ (or END₂) which leads to high \mathcal{R} and D for the hybrids. The \mathcal{R} , D, and EOE of the END₁-graphene hybrid reached values exceeding $\sim 10^9$ A W⁻¹, $\sim 10^{15}$ Jones, and $\sim 10^9$ %, respectively. Similarly, the END₂-graphene hybrid exhibited values for \mathcal{R} , D, and EQE of $\sim 10^8$ A W⁻¹, $\sim 10^{14}$ Jones, and $\sim 10^6$ %, respectively. Moreover, the optoelectronic response of the END2graphene hybrids showed a broadband response well into the IR up to 1100 nm, unlike the END₁-graphene hybrids where the photoresponse decreased for $\lambda \gtrsim 850$ nm. To the best of our knowledge, our results represent the first approach towards the fabrication of an endohedral fullerene-graphene-based photodetectors, which does not require a complicated fabrication process and yields the highest reported values for photodetector device figures of merit. The excellent performance of our endohedral-fullerene graphene hybrid photodetectors is exceptional and is bound to pave the way for a new class of hybrid 0D-2D graphene-based photonic devices in the future for imaging, surveillance and defense-related applications.

4. Methods

Materials

A $10 \times 10 \times 1$ mm HOPG crystal from SPI Supplies Grade SPI-1 was mechanically exfoliated on top of a SiO2/Si substrate using residue-free blue tac tape from Semiconductor Corp resulting in a few layer graphene (FLG) membrane. The procedure for exfoliation adopted was similar to that described by Saenz et al. 60 A suspension of endohedral END₁ (Sc₃N@C₈₀) (LUNA LnW-0920, END₁ Trinetasphere, $\gtrsim 95\%$) at different concentrations in ~ 1 mL of o-DCB was electrophoretically deposited on the graphene membrane. Endohedral END₂ (La@C₈₂) was prepared using a Krätschmer–Huffman arc discharge generator and purified using HPLC after extracting the soot with toluene as previously described. 28,59

4.2 Characterization

Optical absorption spectroscopy was conducted using a CARY 5000 spectrophotometer in quartz cuvettes with $\sim\!0.3$ mL volumetric capacity. The SEM imaging was carried out with a Hitachi S-4800. For AFM, the images were acquired using a Veeco Microscope at ambient air conditions (relative humidity $\sim\!30\%$) with $k\sim0.3$ N m $^{-1}$ for the silicon tip (provided by Ted Pella Inc.) in contact mode. The Raman data was gathered using a Horiba LabRAM HR Evolution, where the excitation λ used was $\sim\!532$ nm.

4.3 Device fabrication and measurements

The devices were fabricated using a photolithography process for metal contact patterning on a \sim 270 nm SiO₂/Si substrate. The electrodes were patterned on a graphene membrane using a Karl Suss MJB3 mask aligner. 60 Then, ~10 nm of Ti and ~100 nm of Au were deposited using an e-beam evaporator, followed by metal lift-off. The electronic and optoelectronic device characterization was conducted using a Lakeshore CRX-4K cryogenic probe stage with T control from ~ 5.8 K to 298 K and a low noise semiconductor parameter analyzer, the Keysight B1500A was used for the low-noise electronic transport measurements. The photoresponse was measured at room T by illuminating the device with a broadband light source (LEDR/4 type illuminator) which has a color T of ~ 6500 K. The tunable spectral measurements from $T \sim 5.8$ K to ~ 298 K were conducted using a tunable laser source, the Fianium LLFT Contrast from NKT Photonics. Both the broadband and narrow-band sources were calibrated using the Thorlabs optical power meter PM100D.

Conflicts of interest

There are no conflicts to declare.

Acknowledgements

We would like to thank Ben Sarota and Sangram Mazumder at UNT who assisted with the Au/Ti deposition. We greatly appreciate the support received from the Air Force Office of Scientific Research (grant number FA9550-15-1-0200), the Army Research Office (grant number W911NF-15-1-0425) and the National Science Foundation (grant number NSF ECCS 1753933) that enabled us to pursue this work. A. B. K. is also grateful to the support

received from the UNT Start-up package and the PACCAR Technology Institute and Endowed Professorship. L. E. thanks the NSF for generous support of this work under grant (CHE-1801317) and to the NSF-PREM program (DMR-1205302). The Robert A. Welch Foundation is also gratefully acknowledged for an Endowed Chair to L. E. (grant AH-0033).

References

- 1 F. Bonaccorso, Z. Sun, T. Hasan and A. C. Ferrari, *Nat. Photonics*, 2010, 4, 611.
- 2 K. S. Novoselov, D. Jiang, F. Schedin, T. J. Booth, V. V. Khotkevich, S. V. Morozov and A. K. Geim, *Proc. Natl. Acad. Sci. U. S. A.*, 2005, 102, 10451.
- 3 A. C. Ferrari, F. Bonaccorso, V. Fal'ko, K. S. Novoselov, S. Roche, P. Bøggild, S. Borini, F. H. L. Koppens, V. Palermo, N. Pugno, J. A. Garrido, R. Sordan, A. Bianco, L. Ballerini and J. Kinaret, *Nanoscale*, 2015, 7, 4598.
- 4 Z. Sun, T. Hasan, F. Torrisi, D. Popa, G. Privitera, F. Wang, F. Bonaccorso, D. M. Basko and A. C. Ferrari, *ACS Nano*, 2010, 4, 803.
- 5 A. B. Kaul, J. Mater. Res., 2014, 29, 348.
- 6 H. Zhou, T. Gu, J. F. McMillan, M. Yu, G. Lo, D. L. Kwong, G. Feng, S. Zhou and C. W. Wong, *Appl. Phys. Lett.*, 2016, 108, 1.
- 7 F. Xia, T. Mueller, Y. Lin, J. Tsang and M. Freitag, *Nano Lett.*, 2009, 9, 1039.
- 8 K. Roy, M. Padmanabhan, S. Goswami, T. P. Sai, G. Ramalingam, S. Raghavan and A. Ghosh, *Nat. Nanotechnol.*, 2013, **8**, 826.
- 9 D. Fadil, R. F. Hossain, G. A. Saenz and A. B. Kaul, *J. Mater. Chem. C*, 2017, 5, 5323.
- 10 G. Jnawali, Y. Rao, J. H. Beck, N. Petrone, I. Kymissis, J. Hone and T. F. Heinz, *ACS Nano*, 2015, **9**, 7175.
- 11 C. O. Aristizabal, E. J. G. Santos, S. Onishi, A. Yan, H. I. Rasool, Y. Lv, D. Latzke, J. V. Jr, M. F. Crommie, M. Sorensen, C. Lin, K. Watanabe, T. Taniguchi, A. Lanzara and A. Zettl, ACS Nano, 2017, 11, 4686.
- 12 S. Qin, X. Chen, Q. Du, Z. Nie, X. Wang, H. Lu, X. Wang, K. Liu, Y. Xu, Y. Shi, R. Zhang and F. Wang, *ACS Appl. Mater. Interfaces*, 2018, **10**, 38326.
- J. Correa, P. Orellana and M. Pacheco, *Nanomaterials*, 2017,
 69.
- 14 E. J. G. Santos, D. Scullion, X. S. Chu, D. O. Li, N. P. Guisinger and Q. H. Wang, *Nanoscale*, 2017, 9, 13245.
- 15 J. A. Rather, E. A. Khudaish, A. Munam, A. Qurashi and P. Kannan, *Sens. Actuators, B*, 2016, 237, 672.
- 16 D. Yu, K. Park, M. Durstock and L. Dai, J. Phys. Chem. Lett., 2011, 2, 1113.
- 17 K. Kim, T. H. Lee, E. J. G. Santos, P. S. Jo, A. Salleo, Y. Nishi and Z. Bao, *ACS Nano*, 2015, **9**, 5922.
- 18 B. Kang, Y. Kim, W. J. Yoo and C. Lee, Small, 2018, 14, 1802593.
- 19 R. F. Hossain, I. G. Deaguero, T. Boland and A. B. Kaul, *npj* 2D Mater. Appl., 2017, 1, 28.
- 20 H. Xu, X. Han, X. Dai, W. Liu, J. Wu, J. Zhu, D. Kim, G. Zou, K. A. Sablon, A. Sergeev, Z. Guo and H. Liu, *Adv. Mater.*, 2018, 30, 1706561.

- 21 L. H. Li, T. Tian, Q. Ca1, C. J. Shih and E. J. G. Santos, *Nat. Commun.*, 2018, 9, 1271.
- 22 T. H. Lee, K. Kim, G. Kim, H. J. Park, D. Scullion, L. Shaw, M. Kim, X. Gu, W. Bae, E. J. G. Santos, Z. Lee, H. S. Shin, Y. Nishi and Z. Bao, *Chem. Mater.*, 2017, 29, 2341.
- 23 A. Pinkard, A. M. Champsaur and X. Roy, Acc. Chem. Res., 2018, 51, 919.
- 24 S. Du, W. Lu, A. Ali, P. Zhao, K. Shehzad, W. Yin, J. Luo, B. Yu, T. Hasan, Y. Xu, W. Hu and X. Duan, *Adv. Mater.*, 2017, 29, 1700463.
- 25 A. De Sanctis, G. F. Jones, D. J. Wehenkel, F. Bezares, F. H. L. Koppens, M. F. Craciun and S. Russo, *Sci. Adv.*, 2017, 3, 1602617.
- 26 N. F. Montcada, S. Arrechea, A. Molina-Ontoria, A. I. Aljarilla, P. de la Cruz, L. Echegoyen, E. Palomares and F. Langa, *Org. Electron.*, 2016, 38, 330.
- 27 M. Vizuete, M. Barrejón, M. J. Gómez-Escalonilla and F. Langa, *Nanoscale*, 2012, 4, 4370.
- 28 A. A. Popov, S. Yang and L. Dunsch, Chem. Rev., 2013, 113, 5989.
- 29 M. N. Chaur, F. Melin, A. L. Ortiz and L. Echegoyen, *Angew. Chem.*, *Int. Ed.*, 2009, 48, 7514.
- 30 J. U. Reveles, N. N. Karle, T. Baruah and R. R. Zope, J. Phys. Chem. C, 2016, 120, 26083.
- 31 J. R. Pinzón, D. C. Gasca, S. G. Sankaranarayanan, G. Bottari, T. Torres, D. M. Guldi and L. Echegoyen, *J. Am. Chem. Soc.*, 2009, **131**, 7727.
- 32 I. Jeon, H. Ueno, S. Seo, K. Aitola, R. Nishikubo and A. Saeki, *Angew. Chem.*, 2018, **130**, 4697.
- 33 R. B. Ross, C. M. Cardona, D. M. Guldi, S. G. Sankaranarayanan, M. O. Reese, N. Kopidakis, J. Peet, B. Walker, G. C. Bazan, E. Van Keuren, B. C. Holloway and M. Drees, *Nat. Mater.*, 2009, 8, 208.
- 34 M. Liedtke, A. Sperlich, H. Kraus, A. Baumann, C. Deibel, M. J. M. Wirix, J. Loos, C. M. Cardona and V. Dyakonov, *J. Am. Chem. Soc.*, 2011, 133, 9088.
- 35 Y. Xu, J. Guo, T. Wei, X. Chen, Q. Yang and S. Yang, *Nanoscale*, 2013, 5, 1993.
- 36 S. Nagase and K. Kdmyashi, Chem. Phys. Lett., 1994, 231, 319.
- 37 K. Harigaya and S. Abe, *Phys. Rev. B: Condens. Matter Mater. Phys.*, 1994, **49**, 16746.
- 38 S. Stevenson, G. Rice, T. Glass, K. Harlch, F. Cromer, M. R. Jordan, J. Craft, E. Hadju, R. Bible, M. M. Olmstead, K. Maltra, A. J. Fisher, A. L. Balch and H. C. Dorn, *Nature*, 1999, 401, 55.
- 39 S. Lebedkin, B. Renker, R. Heid, H. Schober and H. Rietschel, *Appl. Phys. A: Mater. Sci. Process.*, 1998, **66**, 273.

- 40 Y. Takano, Fullerenes, Nanotubes, Carbon Nanostruct., 2014, 22, 243.
- 41 M. Rudolf, S. Wolfrum, D. M. Guldi, L. Feng, T. Tsuchiya, T. Akasaka and L. Echegoyen, *Chem. Eur. J*, 2012, **18**, 5136.
- 42 A. C. Ferrari, J. C. Meyer, V. Scardaci, C. Casiraghi, M. Lazzeri, F. Mauri, S. Piscanec, D. Jiang, K. S. Novoselov, S. Roth and A. K. Geim, *Phys. Rev. Lett.*, 2006, 97, 1.
- 43 S. Tian, Y. Yang, Z. Liu, C. Wang, R. Pan, C. Gu and J. Li, Carbon, 2016, 104, 27.
- 44 I. Calizo, A. A. Balandin, W. Bao, F. Miao and C. N. Lau, Nano Lett., 2007, 7, 2645.
- 45 B. Davaji, H. D. Cho, M. Malakoutian, J. K. Lee, G. Panin, T. W. Kang and C. H. Lee, *Sci. Rep.*, 2017, 7, 1.
- 46 J. Schiefele, F. Sols and F. Guinea, Phys. Rev. B: Condens. Matter Mater. Phys., 2012, 85, 195420.
- 47 Y. Liu, Z. Liu, W. Lew and Q. Wang, *Nanoscale Res. Lett.*, 2013, 8, 335.
- 48 M. Michel, C. Biswas, C. S. Tiwary, G. A. Saenz, R. F. Hossain, P. Ajayan and A. B. Kaul, 2D Mater., 2017, 4, 025076.
- 49 D. Zhang, L. Gan, Y. Cao, Q. Wang, L. Qi and X. Guo, Adv. Mater., 2012, 24, 2715.
- 50 P. H. Chang, S. Y. Liu, Y. B. Lan, Y. C. Tsai, X. Q. You, C. S. Li, K. Y. Huang, A. S. Chou, T. C. Cheng, J. K. Wang and C. I. Wu, *Sci. Rep.*, 2017, 7, 1.
- 51 H. Qiao, J. Yuan, Z. Xu, C. X. Pan, S. Li and Q. Bao, ACS Nano, 2015, 9, 1886.
- 52 A. Sharma, R. Kumar, B. Bhattacharyya and S. Husale, *Sci. Rep.*, 2016, **6**, 1.
- 53 J. P. Phillips, B. Koene and S. R. Wilson, *Luna innovations*, *US Pat.*, 20080085234, 2008.
- 54 A. Das, S. Pisana, S. Piscanec, B. Chakraborty, S. K. Saha, U. V. Waghmare, R. Yiang, H. R. Krishnamurhthy, A. K. Geim, A. C. Ferrari and A. K. Sood, *Nat. Nanotechnol.*, 2007, 3, 1.
- 55 C. Bautista-Flores, R. Y. Sato-Berrú and D. Mendoza, *J. Mater. Sci. Chem. Eng.*, 2015, **3**, 17.
- 56 C. Casiraghi, S. Pisana, K. S. Novoselov, A. K. Geim and A. C. Ferrari, Appl. Phys. Lett., 2007, 91, 12.
- 57 K. Shibata, Y. Rikiishi, T. Hosokawa, Y. Haruyama, Y. Kubozono, S. Kashino, T. Uruga, A. Fujiwara, H. Kitagawa, T. Takano and Y. Iwasa, *Surf. Sci.*, 2003, 522, 1.
- 58 S. Pang, H. N. Tsao, X. Feng and K. Mullen, *Adv. Mater.*, 2009, 21, 3488.
- 59 T. Akasaka, T. Wakahara, M. Kako, Y. Nakadaira and R. Nagahata, J. Am. Chem. Soc., 2000, 122, 9316.
- 60 G. A. Saenz, G. Karapetrov, J. Curtis and A. B. Kaul, *Sci. Rep.*, 2018, 8, 1.